Journal of Molecular Structure 1229 (2021) 129846

Contents lists available at ScienceDirect

Journal of Molecular Structure

journal homepage: www.elsevier.com/locate/molstr

Cd doped-Alpha-Dimanganese Trioxide Nanoparticles: Synthesis, Structural, Morphological, Optical, Luminescent, Magnetic, Photocatalytic and Antibacterial Characterization

S. Gnanam[a,*], J. Gajendiran[b,*], R. Ashokkumar[c], K. Ramachandran[d], J. Ramana Ramya[e]

[a] Department of Physics, School of Basic Sciences, Vels Institute of Science, Technology & Advanced Studies (VISTAS), Pallavaram, Chennai-600 117, Tamilnadu, India
[b] Department of Physics, Vel Tech Rangarajan Dr.Sagunthala R&D Institute of Science and Technology, Avadi, Chennai 600 062, India
[c] Department of Chemistry, Kumaraguru College of Technology, Chinnavedampatty, Coimbatore 641049, Tamilnadu, India
[d] Department of Physics, SRMIST, Vadapalani Campus, Chennai- 600026, India
[e] National Center for Nanoscience and Nanotechnology, University of Madras, Chennai-600025, Tamilnadu, India

ARTICLE INFO

Article history:
Received 19 October 2020
Revised 20 December 2020
Accepted 23 December 2020
Available online 29 December 2020

Keywords:
Nanostructured materials
Structural properties
Optical properties
Magnetic properties
Photocatalyst
Antibacterial activity

ABSTRACT

In this paper, we present Cd doped alpha-dimanganese trioxide (Cd-A-DMTO) nanoparticles developed with the particle size of 25-28 nm via the sol-gel technique. The effects of 1-3% Cd concentrations on the crystal structure, size and strain, lattice constant, interplanar distance and unit cell volume values of the alpha-dimanganese trioxide (α-Mn_2O_3) samples were compared with the powder X-ray diffraction (XRD) results. The crystallite sizes are computed using the Scherrer's formula and the Williamson-Hall (W-H) plot using the XRD data for the Cd-A-DMTO samples, and their values are comparatively discussed. The powder XRD, and Raman spectral studies have shown the formation of the single crystalline cubic bixbyite phase of the prepared Cd-A-DMTO samples. Structural behaviour was investigated for the prepared Cd-A-DMTO samples by the Fourier Transform Infrared (FT-IR). The energy dispersive X-ray (EDX) analysis shows that the Cd has been incorporated into the manganese oxide. The spheres/rods, spindles/spheres and hexagonal/sphere-like particles are found in the 1%, 2% and 3% Cd-A-DMTO samples in the Scanning Electron Microscopy (SEM) and Transmission Electron Microscopy (TEM) analyses. Superparamagnetic behavior of the Cd-A-DMTO samples was detected by the Vibrating Sample Magnetometer (VSM). The optical band gap increased and the PL emission intensity decreased with an increase in the concentration of the Cd dopant on the manganese oxide samples in the UV absorption and photoluminescence (PL) emission spectra. The photodegradation of the Congo red (CR) dye showed that the 3% Cd-A-DMTO photocatalyst had greater photocatalytic degradation efficiency and a rate constant compared to the 1% Cd-A-DMTO sample. The antibacterial activity of the Cd-A-DMTO samples was examined using selected bacterial pathogens.

1. Introduction

In the past few years, great efforts have been made to prepare doped nanoparticles for use in transition metal oxides due to their enhancing the optical, luminescent, magnetic, catalytic and electrochemical properties resulting in their potential applications in optoelectronic devices, photocatalysis, antimicrobial activities, supercapacitors and gas sensors [1-29]. It is well-known that the surface to volume ratio (i.e. more numbers of atoms active in site) and imperfection defects (surface defects) play a major role in the photoluminescent, catalytic and biological (antibacterial) properties of metal oxides. As a result, the dopant loading of metal oxides and/or transition metals causes surface defects. This also influences the opto-electronic properties, and the light absorption is likely to shift towards the visible region. Recently, cubic bixbyite type α-Mn_2O_3 nanoparticles have received a lot of attention due to their improved structural, magnetic, optical, photocatalytic and antibacterial activities.

Ramarajan et al. [30] reported that the cubic and chain-like morphology of α-Mn_2O_3 was synthesized using the sol-gel method by mixing manganese chloride, hexamine, and caustic soda in the presence of water. They examined the influence of surfac-

* Corresponding authors.
E-mail addresses: gnanam.physics@gmail.com (S. Gnanam), gaja.nanotech@gmail.com (J. Gajendiran).

https://doi.org/10.1016/j.molstruc.2020.129846
0022-2860/

tants on the microstructural behavior of α-Mn_2O_3 nanostructures with a particle size range of 58-68 nm. Chen et al. [31] reported that α-Mn_2O_3 nanorods were fabricated by taking chemicals such as manganese chloride, potassium permanganate and cetyl trimethyl ammonium bromide (CTAB) as surfactants via the hydrothermal method. They studied the structural properties of α-Mn_2O_3 nanorods. In addition, they found the size of α-Mn_2O_3 material to be 36 nm in diameter and 1μm in length. Liu et al. [32] reported the diameter of 2-3 μm and thickness of 100-250 μm of α-Mn_2O_3 nanoplates by using manganese acetate and polyvinyl pyrrolidone (PVP) as surfactants in the presence of an alcohol solvent (ethylene glycol) via the solvothermal method. In addition, they examined the microstructural properties of α-Mn_2O_3. Yu et al. [33] reported the preparation of α-Mn_2O_3 microspheres by dispersing inorganic salt (manganese nitrate) in ethylene glycol and nitric acid via the solvothermal process. They elucidated the crystalline phase structure, internal surface morphology and electrochemical behavior of α-Mn_2O_3 microspheres. Moreover, they found the diameter to be ~18 μm.

Various metals such as Mo, Cu, Ag, Co, Cr, Fe, In and Nd have been successfully doped into Mn_2O_3 materials using co-precipitation, thermal decomposition, sol-gel accompanied solvothermal, microwave, hydrothermal, sol-gel and electrodeposition methods and their structural and physico-chemical properties have been investigated for potential applications such as photocatalysts, supercapacitors and spintronic devices etc [34-41]. Based on the above-mentioned literature, we could see that large α-Mn_2O_3 particle sizes and mixed crystalline phase were found. In addition, an inert atmosphere, special instruments such as electrodeposition setup, microwave oven, autoclave, high temperature reaction and long reaction synthesis time for Mn_2O_3 material synthesis were needed. In the present work, we have reported that Cd-A-DMTO nanoparticles with an average particle size of 25-28 nm have been obtained, employing the sol-gel method. In addition, the sol-gel process has several advantages over other methods: i.e., there is no need for an autoclave; also, short time reaction synthesis, cheapness of materials, good phase purity, lesser particle size, high yielding powders, precise control of the doping level and so on [12].

In recent years, a few researchers have reported on the enhanced photocatalytic and antibacterial properties of Cd doped and Cd based oxide and sulphide compound nanomaterials [42-47]. Since light radiation interacts with Cd-based materials, better optical absorption has been shown in the optical spectra and its properties of hydrogen peroxide production and therefore the organic dyes are degraded.

To the best of our knowledge, there is no report on the impact of Cd doping on the size and shape of the particles, and the opto-magnetic properties of α-Mn_2O_3 nanoparticles. In addition, the photocatalytic degradation of the CR dye is investigated using a Cd-A-DMTO sample as a photocatalyst. The antibacterial activity of 3% Cd-A-DMTO nanoparticles against bacterial pathogens has been examined for the first time.

2. Experimental

2.1. Materials

Manganese dichloride tetrahydrate ($MnCl_2.4H_2O$) ((Merck), cadmium chloride ($CdCl_2$) (Merck), methanol (CH_3OH) and ammonium hydroxide (NH_4OH) (Merck) were obtained commercially and used as- received without further purification.

2.2. Preparation of Cd-doped A-DMTO nanopowders

1.97g of manganese dichloride tetrahydrate ($MnCl_2.4H_2O$) salt and 1-3 mole % of white crystalline compound of cadmium chloride ($CdCl_2$) were dispersed in 100 mL of colourless liquid methanol (CH_3OH) to form a sol solution under vigorous stirring. In addition to that, 12 mL of colourless ammonium hydroxide (NH_4OH) was added drop wise under continuous magnetic stirring to form a gel network. Further, the filtered opal gels were dried at 120 °C for 15hrs. Finally, brown colored Cd-A-DMTO nanopowders are formed, when calcined at 400 °C for 2hrs. The synthesis process of the pure α-Mn_2O_3 sample is given in the Supporting information.

The feasible formation mechanism of Cd-A-DMTO nanoparticles is given as a chemical reaction below: [30].

$$2MnCl_2 + 4NH_4OH + X_{(1-3\%)}CdCl_2 \rightarrow X_{(1-3\%)}Cd[2Mn(OH)_2] + 4NH_4Cl \quad (1)$$

$$X_{(1-3\%)}Cd[2Mn(OH)_2] + (1/2)O_2 \rightarrow X_{(1-3\%)}Cd[2MnOOH](\text{unstable}) + H_2O \quad (2)$$

$$X_{(1-3\%)}Cd\,[2MnOOH] \rightarrow X_{(1-3\%)}Cd - \alpha - Mn_2O_3 + H_2O \quad (3)$$

2.3. Characterization

Model Schimadzu: X-ray diffractometer (XRD) 6000 instrument detected an angle of diffraction (2θ) of 10-80° using CuKα mediated radiation (wavelength λ= 1.54 Å) and measured the crystallite size and structure of the prepared Cd-A-DMTO samples. Model Bruker IFS 66 V FTIR spectrometer was noted in the wavenumber range 450-4000 cm^{-1} and applied to detect chemical bonding and functional groups of the as-prepared dried powder. Bruker RFS 27: stand-alone model Raman spectrometer (solid state laser source is neodymium-doped yttrium aluminum garnet (Nd: YAG) using wavelength 1064 nm) recorded the wavenumber region of 400-800 cm^{-1} and found the crystal structure of the doped samples. JEOL, JSM-67001 microscope (SEM/EDX) examined the surface morphology and chemical elements of the prepared doped samples. H-800-TEM (Hitachi, Japan) instrument applied an accelerated voltage of 100 kV and measured the effect on the particle size of the doped samples. EG&G PARC-Vibrating sample magnetometer (VSM) 155 model recorded the applied magnetic field range as -10000 to 10000Oe. The Varian Cary 5E spectrophotometer measured the spectral region of 200-800 nm and determined the optical band gap values of the doped samples. The Fluoromax-4 PL spectrofluorometer attached with the Xenon lamp as an excitation optical source in the wavelength range of 410-480 nm was used to investigate the emission behavior and vacancy defects of the prepared doped samples.

2.4. Photocatalytic experimental details

The photocatalytic response was conducted using the degradation of the CR dye/Cd-A-DMTO photocatalyst with the assistance of the Heber-Multilamp photoreactor to find the complete degradation irradiation time. The Hitachi U-2000 double beam UV-vis spectrophotometer analyzed the samples taken at various time intervals and compared the degradation irradiation time of the 1% and 3% Cd-A-DMTO samples. The prepared Cd-A-DMTO catalyst was well mixed with the CR dye solution and transferred to the cylindrical glass reactor. After that, the photodegradation occurred by continuous illumination of the UV-visible light radiation passing through the Cd-A-DMTO catalyst/CR dye solution. The photodegradation process was performed for a period of 120 min for the CR dye, including the first 30 minutes during which the lamp

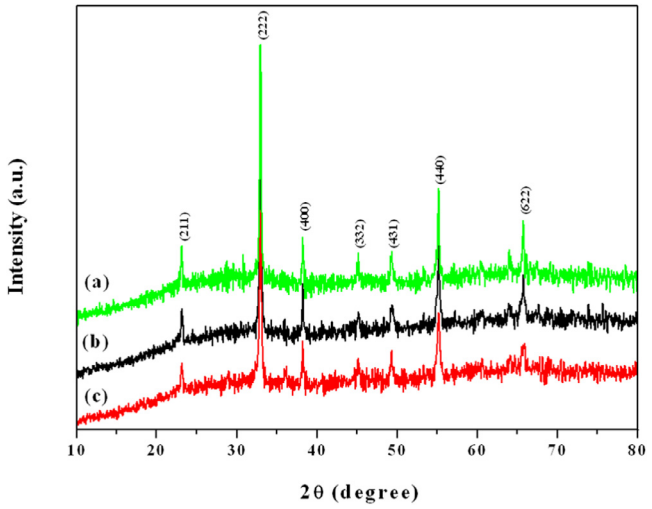

Fig. 1. XRD pattern of (a) 1%, (b) 2% and (c) 3% Cd-A-DMTO.

was switched off for an adsorption-desorption equilibrium. 2 mL CR/catalyst degradation solution was taken every 30 minutes and separated from the solution by centrifuging from the above suspensions. The reaction parameters, such as the initial concentration, the weight of the catalyst, light intensity and the time taken for degradation, are shown in Table S1 (Supporting Information).

2.5. Antibacterial experiment details

The antibacterial efficacy of various concentrations of the 3% Cd-A-DMTO samples' viz. 50, 75 and 100 µg/mL was tested against the gram-positive pathogens (S. aureus, B. subtilis) and gram-negative species (E. Coli, P. aeruginosa and P. mirablis) using the agar well-diffusion process. The well diffusion test was conducted using the Mueller Hinton Agar (MHA) medium containing the nutrient agar in triple distilled water. The medium was prepared and autoclaved at a pressure of 15 lbs (121°C) for 15 minutes. The medium was poured for a uniform depth of 4 mm, equivalent to approximately 25 mL in a 90 mm sterile petri plate. The sterile swab was used to swipe the surface of the MHA medium to ensure an even distribution of the inoculums. The bacterial suspension of 10 μL was evenly distributed over the agar plates. A sterilized 9 mm cork borer was used to make the agar wells. Samples were dissolved with 100% Dimethyl sulfoxide (DMSO). 25, 75 and 100 μL of diluted test compound stock solutions were put in each well and 100% DMSO was regulated. Tetracycline, a well-known antibiotic, is used as a standard. The plates have been incubated at 37°C for 24 hours. The inhibition zone has been measured. The experiment was performed in triplicate.

3. Results and discussion

3.1. Powder X-ray diffraction (XRD)

Powder XRD patterns of the Cd-A-DMTO samples calcined at 400°C are shown in Fig. 1 (a-c). All the reflection planes and their corresponding peak positions match perfectly with the cubic bixbyite phase of α-Mn_2O_3 (JCPDS card no. 41-1442). Furthermore, no additional peaks of impurities, such as cadmium oxide or other manganese oxides are observed, indicating the high purity of the products. The diffraction angle, reflection plane and full width half maximum (FWHM) values of the 1-3% Cd-A-DMTO samples are shown in Table 1. Using Scherrer's equation, the average crystallite sizes are computed to be 28.5, 27.6, and 25.2 nm, respectively for

Table 1
Diffraction angle, reflection plane and FWHM values of the 1-3% Cd-A-DMTO samples.

(hkl) planes	Samples 1% Cd-A-DMTO		2% Cd-A-DMTO		3% Cd-A-DMTO	
	2θ	FWHM	2θ	FWHM	2θ	FWHM
(211)	25.14°	0.206	23.13°	0.309	23.11°	0.386
(222)	33.01°	0.319	32.94°	0.321	32.96°	0.360
(400)	38.22°	0.239	38.22°	0.266	38.21°	0.245
(332)	45.16°	0.328	46.06°	0.310	45.12°	0.309
(431)	49.37°	0.311	49.31°	0.335	49.30°	0.357
(440)	55.16°	0.243	55.16°	0.387	55.14°	0.398
(622)	65.74°	0.354	63.04°	0.378	65.75°	0.434

the 1%, 2% and 3% Cd concentrations doped α-Mn_2O_3 nanocrystals from the high intensity of the diffraction planes (222) in the XRD pattern. Slightly increased broad peaks were observed on increasing the Cd dopant concentration in the α-Mn_2O_3. Increased broad diffraction peaks, specify the decreasing crystallite size. In addition, we have prepared pure α-Mn_2O_3, coloured metals like 3% of Ni, Cu and Ag doped α-Mn_2O_3 materials and the corresponding samples were tested by the XRD, as shown in Fig. S1 (Supporting Information). We found the average crystallite sizes to be 36.2, 38.5, 43.3 and 46.8 nm for the pure, Ni, Cu and Ag doped α-Mn_2O_3 samples respectively, in the XRD pattern. Average crystallite size histogram of pure and doped alpha-dimanganese trioxide nanoparticles as shown in Fig. S2 (Supporting Information). We could infer that the Cd-A-DMTO samples have controlled sizes compared to those of pure, Ni, Cu and Ag doped α-Mn_2O_3 material. In addition, from the XRD pattern of the pure α-Mn_2O_3 sample, we found the average crystallite size to be large. Further, we detected the impurity phase for the prepared coloured metals like Ni, Cu and Ag doping of α-Mn_2O_3 samples in the XRD and its consequence formed the mixed crystalline phase with increased crystallite size, as shown in the Supporting Information. In the present work, we have concentrated on the size controlled and single phase of α-Mn_2O_3 for the photocatalytic and antibacterial applications. Hence, we have chosen 1-3% Cd-A-DMTO for the photocatalytic and antibacterial applications.

In addition, from Table 2, it is observed that the d-spacing, lattice constant and unit cell volume values decreased from 1% to 3% of the Cd-A-DMTO samples. Further, the lattice constant of the obtained 1-3% Cd-A-DMTO samples matched closely with the previous report of the α-Mn_2O_3 materials [8].

For the 1-3% Cd-A-DMTO samples, we plotted 4sinθ on the x-axis and β_{hkl} cosθ on the y-axis, using powder XRD data from the W-H plot (Fig. S3, Supporting Information) to analyze the crystallite size and strain values. The values of the crystallite size and crystalline strain were found to be derived from the slope and intercept fit curve, respectively, by taking the W-H plot. These values (obtained from the W-H plot), which are comparable to the calculated crystallite size using Scherrer's formula, are shown in Table 3. Furthermore, Table 3 shows that the crystallite size decreased and the strain values increased, with an increase in the concentration of the Cd dopant in α-Mn_2O_3.

3.2. Fourier Transform Infrared (FTIR)

The FTIR spectra of the as-prepared 1-3% Cd-A-DMTO samples dried at 120 °C are displayed in Fig. 2(a-c). The broad peak detected at ~1612 and 3415 cm^{-1}, is due to the adsorbed water and stretching vibrations of the hydroxyl (OH) groups [48]. In addition, the strong broad band that appears at the wavenumber 614 and 508 cm^{-1} is attributed to the vibration of the manganese-oxygen (Mn–O) bond [49]. The FT-IR spectrum of the 3% Cd-A-DMTO sample calcined at 400°C for 2hrs is shown in Fig. S4 (Supporting In-

Table 2
Diffraction angle, interplanar distance (d-spacing), lattice constant (a) and unit cell volume values of the 1-3% Cd-A-DMTO samples.

Samples	2θ	$d = n\lambda/2\sin\theta$ (Å)	$a = d \times \sqrt{(h^2+k^2+l^2)}$ (Å)	Volume of the unit cell $(a^3) = V^3$ $(Å)^3$
1% Cd-A-DMTO	33.01°	2.743	9.490	854.67
2% Cd-A-DMTO	32.94°	2.716	9.397	829.78
3% Cd-A-DMTO	32.96°	2.714	9.390	827.93

Table 3
Crystallite size and strain values of the 1-3% Cd-A-DMTO samples.

Samples	Crystallite size in nm is calculated using the Scherrer's equation	Crystallite size in nm is calculated from the W-H plot	Crystallite strain is estimated from the W-H plot
1% Cd-A-DMTO	28.5	23	1.31×10^{-3}
2% Cd-A-DMTO	27.6	20	1.49×10^{-3}
3% Cd-A-DMTO	25.2	18	3.29×10^{-3}

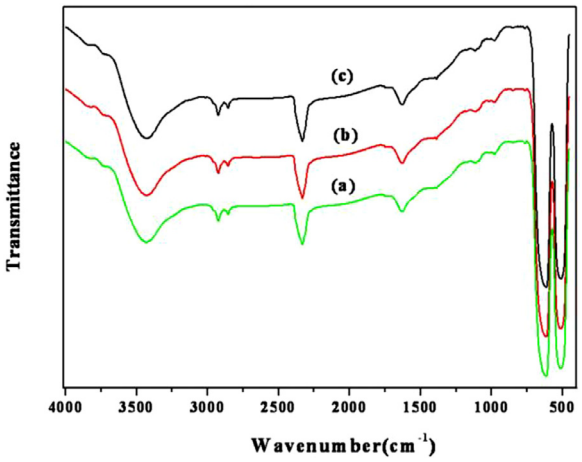

Fig. 2. FTIR spectra of (a) 1%, (b) 2% and (c) 3% Cd-A-DMTO.

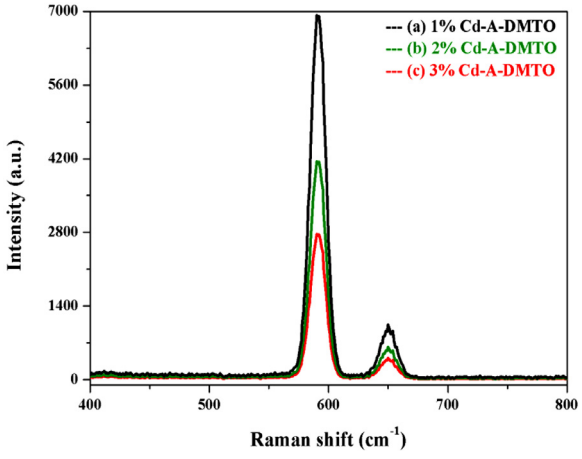

Fig. 3. Raman spectra of (a) 1%, (b) 2% and (c) 3% Cd-A-DMTO.

formation). A broad band located at 646 cm^{-1}, is ascribed to the manganese-oxygen (Mn-O) vibration. Furthermore, no additional bands are detected in the FT-IR spectrum. Thus, the FT-IR analysis of a 3% Cd doped calcined sample confirms the formation of manganese oxide.

3.3. Raman spectra

Fig. 3 (a-c) depicts the Raman spectra of the 1-3% Cd-A-DMTO nanoparticles calcined at 400°C. The strong peaks located at 650 and 590 cm^{-1} are assigned to the vibration of Mn-O, which reveals the cubic bixbyite structure of the Cd-A-DMTO samples. In this analysis, a total of two modes were found in the Cd-A-DMTO samples ranging from 550-700 cm^{-1} [50]. The peak located at 650 cm^{-1} can be correlated with the Ia-3 space group cubic structure with A_{1g} symmetrical Mn-O stretching mode in α-Mn_2O_3 [51]. Furthermore, a small variance of the intensity peaks in the Raman spectra was observed in the 1-3% Cd-A-DMTO samples due to the size and lattice strain effect. The absence of known crystalline phases of CdO in the Cd-A-DMTO samples means that it is finely dispersed in the α–Mn_2O_3 matrix. This observation supports the XRD and FT-IR results.

3.4. Scanning Electron Microscopy (SEM) and Energy Dispersive X-ray (EDX)

Fig. 4(a-c) represents the SEM morphology of the 1%, 2% and 3% Cd-A-DMTO samples. The spheres/rods, spindle/spheres and hexagonal/sphere-like particles are noticed for the 1%, 2% and 3% Cd-A-DMTO samples. Fig. 4 (d) displays the EDX spectrum of the 3% Cd- A-DMTO sample. The strong patterns of manganese (Mn) and oxygen (O) and weak intensity of cadmium (Cd) are traced in the EDX spectrum, confirming that the Cd has been incorporated in the manganese oxide material. In addition, the EDX spectra of the prepared pure α-Mn_2O_3, Ni and Ag doped α-Mn_2O_3 samples (Fig. S5) are displayed in the supporting information.

3.5. Transmission Electron Microscopy (TEM)

Fig. 5 (a-c) presents the TEM images of the 1-3% Cd-A-DMTO samples. The spheres/ rods, spindle/ spheres, and hexagonal/ sphere-like particles are observed for the 1%, 2% and-3% Cd-A-DMTO nanoparticles, which are similar to those, observed in the SEM analysis, as shown in Fig. 4 (a-c). The average particle sizes of the 1%, 2% and 3% Cd-A-DMTO samples are measured to be 28, 27 and 25 nm from the TEM studies, and are well matched with the crystallite sizes, computed by using Scherer's formula from the XRD data. In addition, the obvious several diffraction rings of SAED in the inset of Fig. 5 (a-c) point out that all the products are polycrystalline in nature [52]. The probable schematic formation mechanism of the Cd-A-DMTO samples is displayed in Fig. 5 (d).

Initially, the precursor material (manganese dichloride tetrahydrate) and transition metal dopant (cadmium chloride) were dissolved in a methanol solvent at room temperature under vigorous stirring. Due to the reaction of alcoholysis, cations and anions have been dissociated from manganese and cadmium salt in the methanol solvent to form a sol solution. After that, ammonium hydroxide, as a metal hydroxide precursor, was applied to the above-mentioned sol-solution; the formation of a cadmium-manganese hydroxide gel network was caused by a condensation reaction.

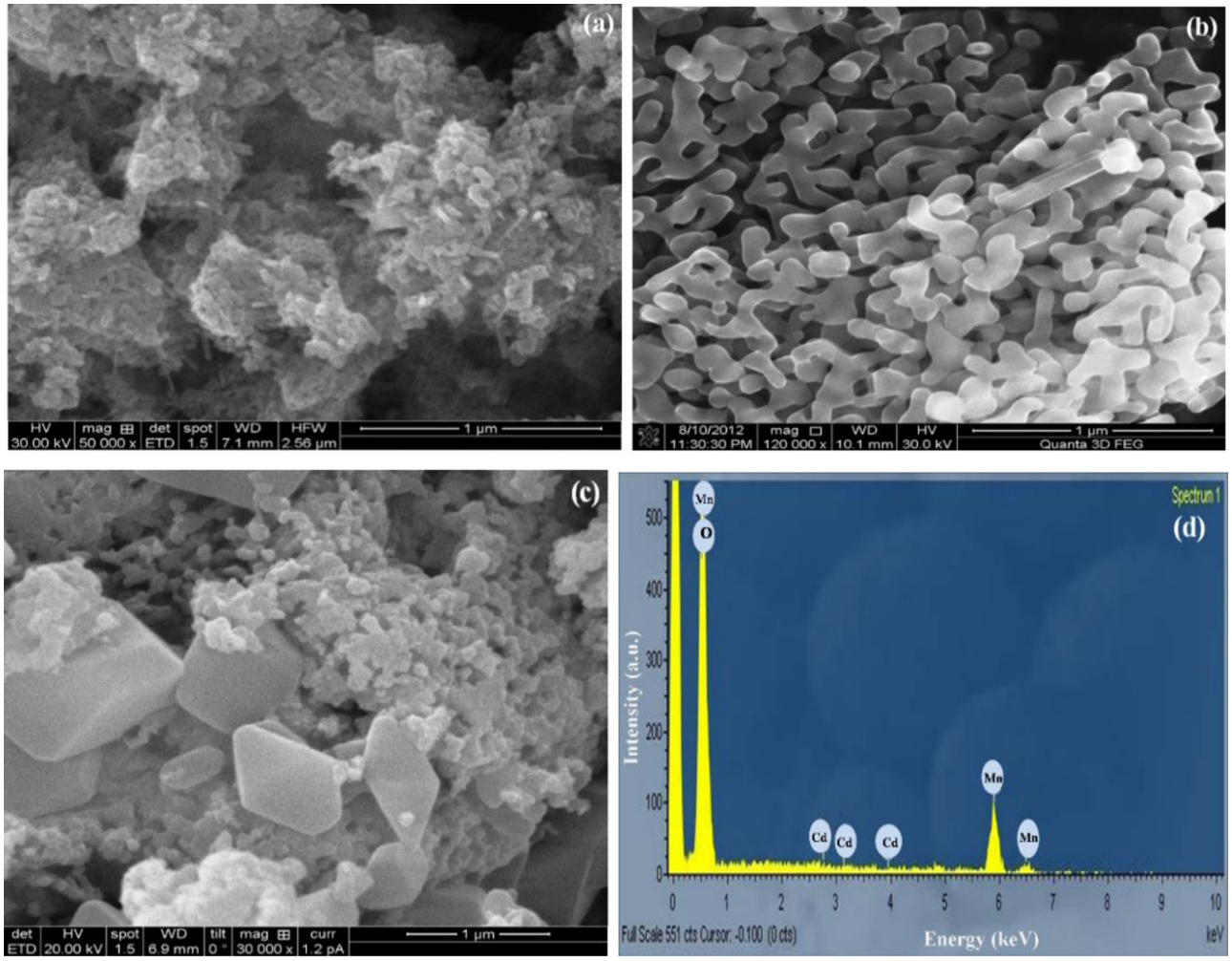

Fig. 4. SEM pictures of (a) 1%, (b) 2%, and (c) 3% Cd-A-DMTO samples; and (d) EDX pattern of Cd-A-DMTO material.

Further, filtered opal gels have been dried to form a cadmium-manganese hydroxide intermediate product. Any residues on the surface of cadmium-manganese hydroxide have been removed during the drying process. As a result, the intermediate compound was converted into metal oxide nanoparticles during the calcination process. In this way, the single crystalline cubic bixbyite pure phase and the Cd-A-DMTO nanoparticles were formed using a simple sol-gel technique.

3.6. Vibrating Sample Magnetometer (VSM) analysis

Fig. 6 (a-c) reveals the room temperature magnetic measurement (magnetization-applied magnetic field (M-H) curve)) of the 1-3% Cd-A-DMTO nanoparticles. It can be observed, that in the samples in which doping has been increased, the magnetization values decreased in the applied fields. This magnetic property of the α-Mn_2O_3 nanoparticles is greatly impacted by the addition of a transition Cd metal ion dopant. In addition, all the doped samples displayed superparamagnetic behavior (S-shape curve). With the potential to produce Cd-A-DMTO with lower magnetization at room temperature, it is a promising material that can be used in future spintronics products.

3.7. UV-Visible Absorption spectroscopy

The optical absorption spectra of the 1-3% Cd-A-DMTO nanoparticles are depicted in Fig. 7 (a-c). In the spectra, the absorption onsets of the samples have been shifted to the lower wavelength region (from the high frequency region) with an increase in the concentration of the Cd dopant. It means that the doping concentration of Cd^{2+} ion increases the energy gap of the α-Mn_2O_3 samples. The band gap energies of the 1%, 2%, 3% concentrations of the Cd doped samples, tallied as 3.57, 3.70 and 3.85 eV from the Tauc plot ($h\upsilon$ on the x-axis vs $(\alpha h\upsilon)^2$ on the y-axis) using optical absorption spectra data, as displayed in the inset of Fig. 7. The tallied energy gap values are larger than that of the bulk [5].

3.8. Photoluminescence (PL) spectroscopy

Fig. 8 (a-c) illustrates the PL emission spectra of the 1-3% Cd-A-DMTO nanoparticles, taken under an excitation wavelength of 325 nm. The PL emission intensity of the α-Mn_2O_3 nanoparticles decreased on increasing the Cd dopant concentration. Specifically, the 3% Cd-A-DMTO sample shows decreased visible emission peaks, more than the other two concentrations. The strong band at 450 nm may be related to the crystal defects associated with the oxygen vacancies, or the Mn interstitial [53]. Generally, the photoluminescent emission intensity is directly related to the photocatalytic activity due to the recombination of the excited electrons and holes. At a lower concentration of Cd dopant in the α-Mn_2O_3 sample, we found higher emission intensity which suggests an increase in the recombination rate of the electrons and holes. Decreased PL intensity with an increase in the Cd doped concentration in α-Mn_2O_3 could be due to the suppression in the recom-

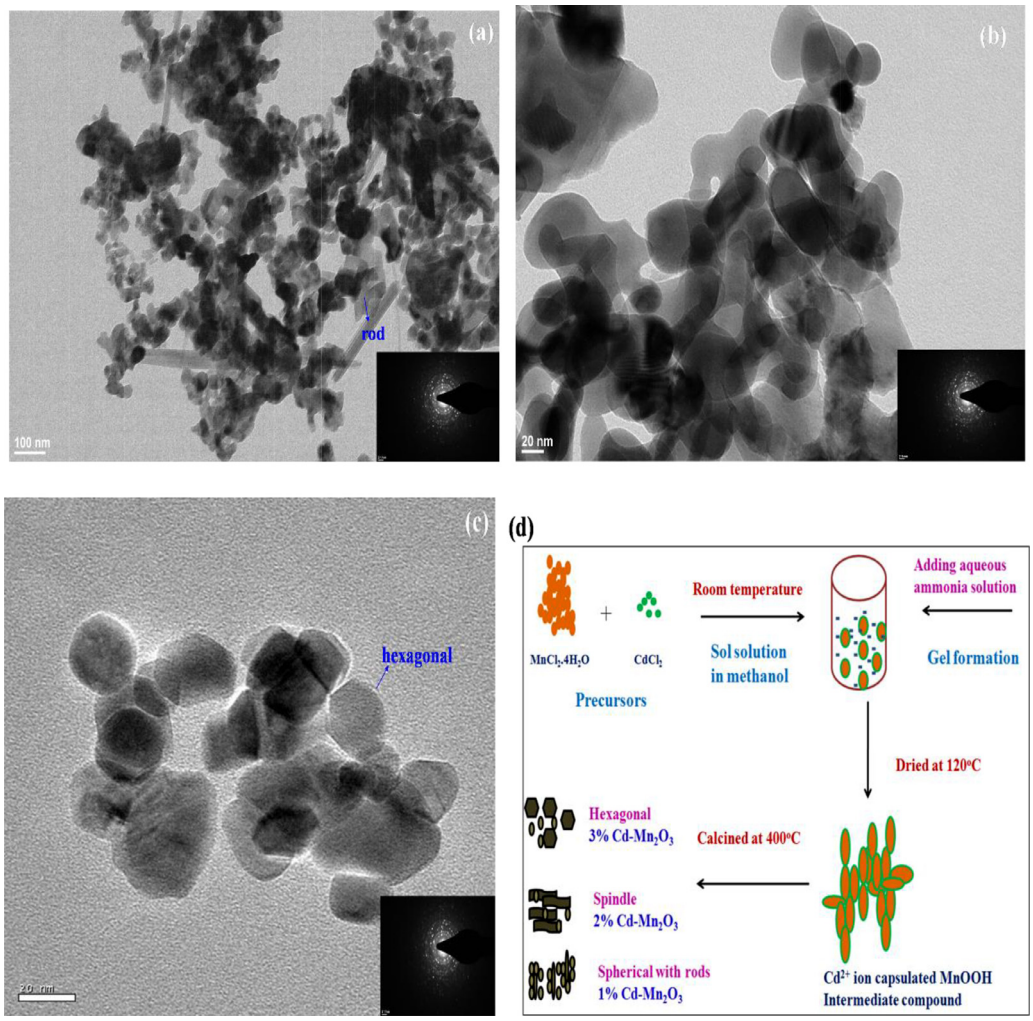

Fig. 5. TEM pictures of (a) 1%, (b) 2% and (c) 3% Cd-A-DMTO samples; (d) Schematic formation mechanism of the Cd-A-DMTO samples.

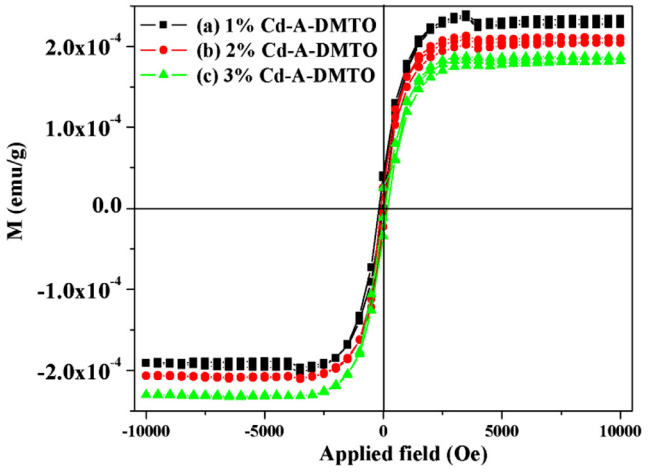

Fig. 6. M-H plots of (a) 1%, (b) 2% and (c) 3% Cd-A-DMTO nanoparticles.

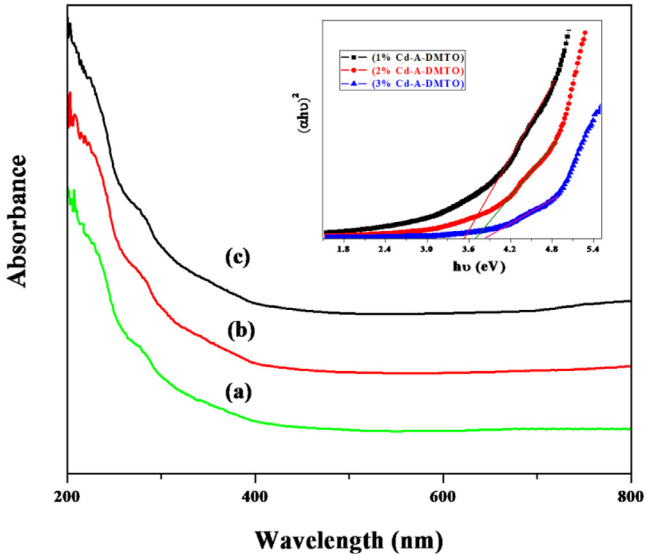

Fig. 7. UV absorption spectra of (a) 1%, (b) 2% and (c) 3% Cd-A-DMTO samples.

bination of the electrons and hole pairs [54] as-a consequence of which more number of free charge carriers participated on the surface of α-Mn_2O_3 to enhance better photocatalytic activity. However, structural defects are caused and, as a result, oxygen vacancy defects are relatively low, compared to those of the 1% and 2% Cd-A-DMTO. Generally, the decrease in PL emission intensity and the controlled size of the particles is a significant factor in enhancing the photocatalytic activity of nanostructured materials [55,56]. As a result, the 3% Cd-A-DMTO sample was tested in the photocatalytic experiment and compared to the 1% Cd-A-DMTO sample.

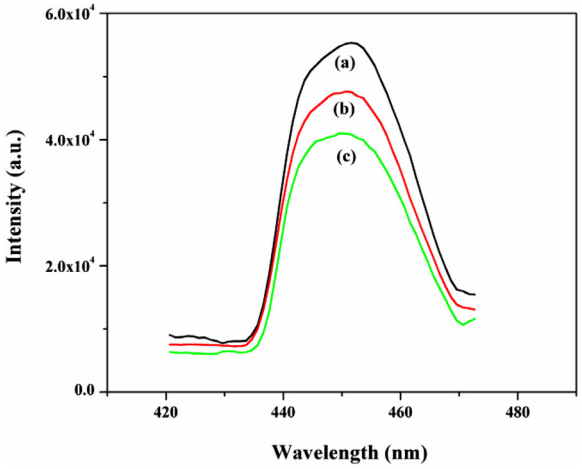

Fig. 8. PL spectra of (a) 1%, (b) 2% and (c) 3% Cd-A-DMTO samples.

3.9. Photocatalytic Activity

The role of the Cd-A-DMTO sample as an efficient photocatalyst is detected using the photodegradation of the CR dye, using UV-visible light at various irradiation time intervals. The photocatalytic activity of the 3% Cd-A-DMTO sample was investigated, and compared with that of the 1% Cd-A-DMTO sample as shown in Fig. 9(a-b). We noticed that the absorption peak decreases with continuously illuminating UV-visible light radiation in the optical absorption spectra, which suggests that the CR dye concentration decreases in the presence of the Cd-A-DMTO samples. The optical absorption peak intensity of the CR dye wavelength at ~495 nm is shown to be substantially reduced within 30 minutes of irradiation and the decoloration of the CR dye is almost completed within 120 minutes for the 3% Cd-A-DMTO catalyst (Fig. 9(b)), while the degradation is closely lost at the end of 120 minutes for the 1% Cd-A-DMTO catalyst, as seen in Fig. 9(a). On raising the irradiation time, the peak slowly became smoother, indicating that there was ample photocatalytic reaction to break the dye's chromophore [57, 58]. The photocatalytic activity of the 3% Cd-A-DMTO sample is higher than that of the 1% Cd-A-DMTO sample, indicating the higher efficiency of the degradation of the sample.

At a lower doping concentration (1%), the Cd ion traps the photo-induced electron and increases the recombination rate of the electron and hole pair in the α-Mn_2O_3 and increases its surface barrier effect. As a result, the electron and hole pair separation is increased and the photocatalytic activity has decreased as a result. At higher concentrations, the Cd (3%) doping ions could capture more photo-induced electrons and suppress the recombination rate of the electron and hole pair in the α-Mn_2O_3 and reduce its surface effect barrier, thereby increasing the photo-catalytic activity of the Cd (3%)-α-Mn_2O_3 sample. In addition, the photocatalytic degradation activity of the pure α-Mn_2O_3 sample (Fig.S6) is shown in the Supporting Information. From Fig.S6, we found that the photocatalytic degradation efficiency of the pure α-Mn_2O_3 sample was 65%. Fig. 9(c) shows the decreasing concentration of the CR dye versus various irradiation time intervals for the Cd-A-DMTO samples. The 3% Cd-A-DMTO sample has a small grain size and large specific surface area, and thus the photoactivity is higher than that of the 1% Cd-A-DMTO.

Fig. 9(d) shows the percentage degradation of the CR dye with Cd-A-DMTO catalysts. In order to compare the efficiency of the catalysts, the % degradation of CR dye was determined to be 85 and 91% for 1% and 3% of the Cd-A-DMTO samples, respectively. The 3% cadmium dopant in the α-Mn_2O_3 nanostructure greatly improves the photoactivity of the CR dye reaction, which may be due to the increased energy transfer. This study shows that the 3% Cd-A-DMTO loaded catalyst was found to be the best. In addition, the irradiation time (min) with -lnC/C_0 was plotted through the linear fit curve to analyze the rate constant of the Cd-A-DMTO catalysts (Fig. 9(e)). The rate constant value was found to be 0.0155/min and 0.0207/min for 1% and 3% of the Cd-A-DMTO samples, respectively, using the kinetics of photocatalytic degradation measured using the pseudo-first order equation below:

$$-\ln(C/C_0) = K \times t \tag{5}$$

Where, k- reaction rate constant, C_o- initial concentration, and C-degradation concentration.

Further, we observed that the R-square values are 0.983 and 0.964 for the 1% and 3% Cd-A-DMTO photocatalyst samples, respectively. Moreover, the half life time can be found as 44.70 and 33.47 min for the 1% and 3% of the Cd-A-DMTO photocatalyst sample using the relationship between the rate constant (K) and half life time ($t_{1/2}$) formula below:

$$t_{1/2} = 0.693/K \tag{6}$$

The entire photocatalytic process of the organic dye degradation is furnished as follows:

$$\text{A-DMTO : Cd} \xrightarrow{h\nu > h\nu_o} e^-| \text{ at CB} + h^+| \text{ at VB} \tag{7}$$

$$h^+| \text{ at VB} + H_2O \rightarrow \bullet OH + H^+ \tag{8}$$

$$h^+| \text{ at VB} + OH^- \rightarrow \bullet OH \tag{9}$$

$$e^-| \text{ at CB} + O_2 \rightarrow \bullet O_2^- \xrightarrow{H_2O} \bullet OOH + OH^-, \tag{10}$$

$$e^-| \text{ at CB} + \bullet OOH \rightarrow H_2O_2 + OH^- \tag{11}$$

$$\bullet OOH + \bullet OOH \rightarrow H_2O_2 + OH^- \tag{12}$$

$$e^-| \text{ at CB} + H_2O_2 \rightarrow \bullet OH + OH^- \tag{13}$$

$$\bullet O_2^- + H_2O_2 \rightarrow \bullet OH + OH^- + O_2 \tag{14}$$

$$\bullet OH + \text{organic dye} \xrightarrow{\text{(via organic intermediates)}} CO_2 + H_2O + \text{inorganic nontoxic products} \tag{15}$$

$$\bullet O_2^- + \text{organic dye} \xrightarrow{\text{(via organic intermediates)}} CO_2 + H_2O + \text{inorganic nontoxic products} \tag{16}$$

The incident photons, having an energy ($h\nu$) greater than the threshold ($h\nu_o$), produce electron-hole pairs on the Cd-A-DMTO nanoparticle surface (Eq. 7); a significant fact of this is that part of the photocatalytic process is due to the suppression of the e^-–h^+ recombination by the charge trapping of the defect levels produced by Cd doping. Depending on the exact conditions, the holes at the valence band (VB), and the electrons at the conduction band (CB) react with water and the adsorbed oxygen to create hydroxyl radicals (•OH) and superoxide anion radicals (O_2•$^-$), respectively, by certain other products such as OH^-, •OOH, H_2O_2, and O_2 (Eq. 9 and 10). Finally, these radicals with a high redox oxidizing ability decompose the CR dye into CO_2, H_2O, and other inorganic nontoxic products (Eq. 16). The cyclic stability test results of the 3% Cd-A-DMTO/CR dye sample (Fig. S7) can be found in the Supporting Information.

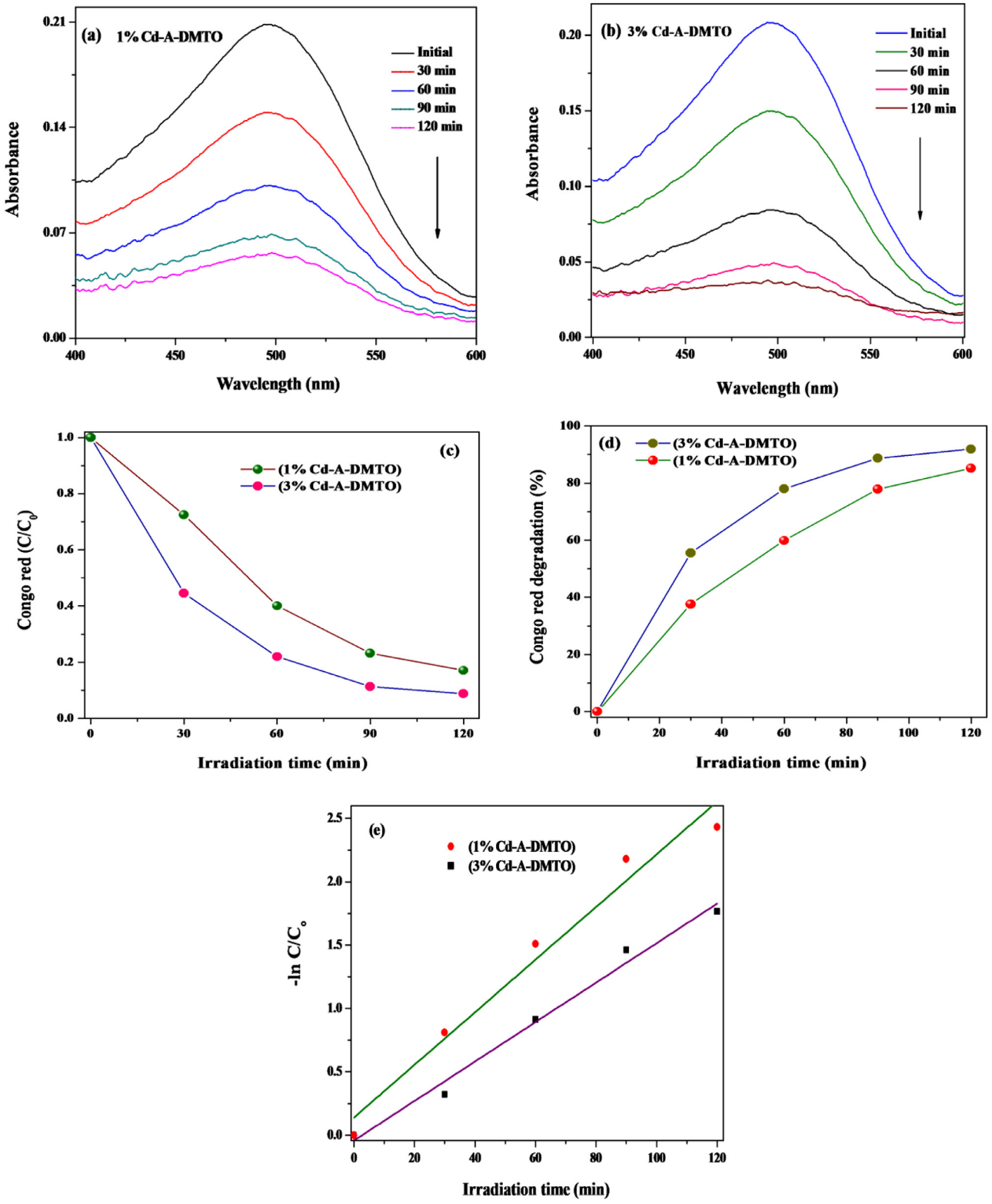

Fig. 9. UV-visible spectra of photodegradation of (a) 1%Cd-A-DMTO and (b) 3% Cd-A-DMTO, (c) Time course of CR dye concentration during photodegradation (d) Degradation percentages of CR dye and (e) ln (C/C_0) versus irradiation time using Cd-A-DMTO catalysts.

3.10. Antibacterial Activity

Fig. 10(A) displays the antibacterial activity histogram of the Cd-A-DMTO nanoparticles against select bacterial pathogens such as *S. aureus, E.coli, B.subtilis, P. aeruginosa* and *P.mirablis* with the agar-well diffusion technique. Tetracycline (S) is used as a positive standard and DMSO (C) is used as a negative control in the experiment (Fig. 10(B)). Among the different bacterial strains, negative strains such as E. coli and P. aeruginosa showed a better inhibition region. Another gram-negative strain of Proteus mirabilis showed a lower

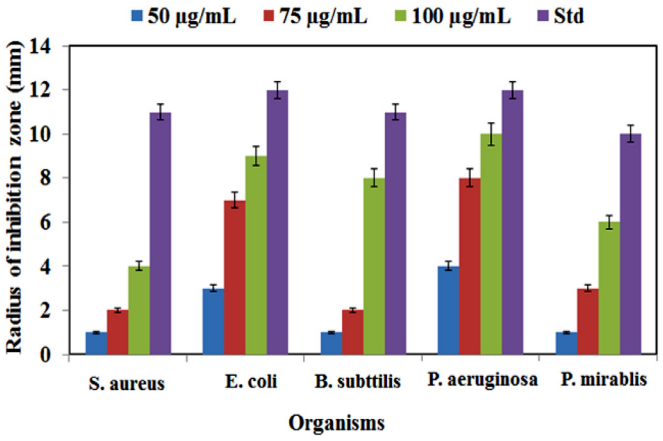

Fig. 10. (A) Antibacterial activities of 3% Cd-A-DMTO sample.

inhibitory effect. Gram-positive strains are more active and have a lower inhibition region. As a result, we may conclude that the samples were more successful against gram-negative strains and could be candidates for such infections. The inhibition zone radius values are measured in mm of the selected bacterial pathogens as shown in Table S3 (Supporting Information). The inhibition zone radius of the 100 µg/mL concentration samples showed 4, 9, 8, 10 and 6 mm for *S. aureus, E.coli, B.subtilis, P. aeruginosa* and *P.mirabilis,* respectively. The findings of antibacterial activity indicate that Cd-A-DMTO nanoparticles acted as excellent antibacterial agents against both gram-positive and gram-negative bacteria [6]. In addition, the antibacterial activity of the pure α-Mn_2O_3 sample (Fig.S8) is explained in the Supporting Information.

The possible mechanism for the antibacterial activity may be nanostructures in which cadmium doped dimanagnese trioxide (from the samples), leaches out and attaches to the cell walls of the bacteria, disrupts the transport of oxygen and affects the active transport of cell membranes resulting in reduced oxidative stress in the bacterial cell. This process contributes to the interruption of enzymatic activity, the transcription of nucleic acids and the cessation of protein synthesis in bacteria leading to their death. It is clear from the findings that Cd-A-DMTO contributes to cell death after a wide distribution of the bacteria [59,60]. Hence, Cd-A-DMTO material can be used as an efficient growth inhibitor in various microorganisms, making it ideal for drug delivery applications.

4. Conclusions

In this work, Cd-A-DMTO nanoparticles are produced through the sol-gel route. The structural (XRD and Raman) studies, revealed the cubic bixbyite phase of Cd-A-DMTO. The chemical bond (Mn-O) and functional groups of the dried samples could be seen in the FT-IR spectra. The spheres/rods, spindle/spheres and hexagonal/sphere-like particles of the 1-3% Cd-A-DMTO nanostructures are observed in the SEM and TEM studies. The magnetization values decreased on increasing the Cd dopant concentration in the α-Mn_2O_3 nanoparticles having a superparamagnetic nature. This has been observed in the M-H curve. The optical band gap energy values are computed using the Tauc plot and the results

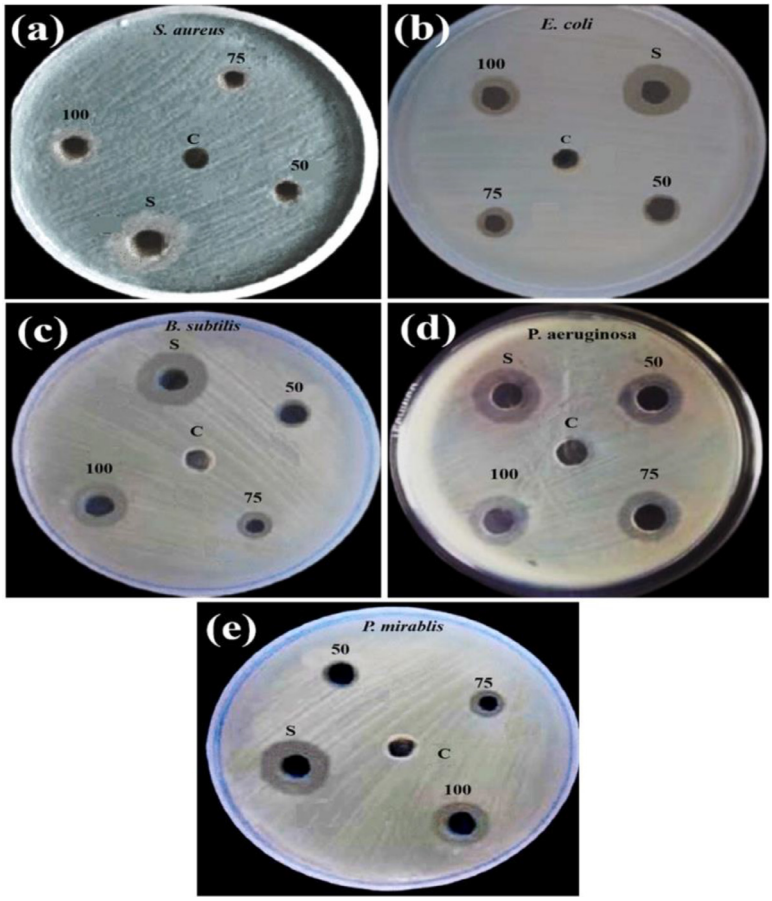

Fig. 10. (B) Antimicrobial efficacy of the Cd-A-DMTO nanoparticles against bacterial pathogens (a) *S. aureus*, (b) *E.coli*, (c) *B.subtilis*, (d) *P. aeruginosa* and (e) *P.mirablis* with various sample concentrations viz. 50, 57 and 100 µL.

have shown that the optical bad gap increases with the concentration of Cd doping. The PL emission characteristics of Cd-A-DMTO showed the dependence of the luminescent intensity on the doping concentration. Based on the above characterization, it can be seen that decreasing particle sizes and magnetization, increasing optical band gaps, and tuning of the surface morphology result on increasing the concentration of the Cd dopant in the case of α-Mn_2O_3. The photocatalytic and antibacterial activities of the Cd-A-DMTO nanoparticles have been discussed in detail.

Declaration of Competing Interest

The authors declare that they have no known competing financial interest or personel relationship that could have appeared to influence the work reported in this paper.

Supplementary materials

Supplementary material associated with this article can be found, in the online version, at doi:10.1016/j.molstruc.2020.129846.

CRediT authorship contribution statement

S. Gnanam: Methodology, Investigation, Writing - original draft, Writing - review & editing. **J. Gajendiran:** Investigation, Writing - original draft, Writing - review & editing, Conceptualization. **R. Ashokkumar:** Formal analysis. **K. Ramachandran:** Formal analysis. **J. Ramana Ramya:** Formal analysis.

References

[1] M.G. Nair, M. Nirmala, K. Rekha, A. Anukaliani, Structural, optical, photocatalytic and antibacterial activity of ZnO and Co doped ZnO nanoparticles, Mater. Lett. 65 (2011) 1797–1800.

[2] T. Ali, Ateeq Ahmed, Umair Alam, Imran Uddin, P. Tripathi, M. Muneer, Enhanced photocatalytic and antibacterial activities of Ag-doped TiO_2 nanoparticles under visible light, Mater. Chem. Phys 212 (2018) 325–335.

[3] S. Thota, T. Dutta, J. Kumar, On the sol-gel synthesis and thermal, structural, and magnetic studies of transition metal (Ni, Co, Mn) containing ZnO powders, J. Phys. Condens. Matter. 18 (2006) 2473–2486.

[4] K. Kaviyarasu, P.P. Murmu, J. Kennedy, F.T. Thema, Douglas Letsholathebe, L. Kotsedi, M. Maaza, Structural, optical and magnetic investigation of Gd implanted CeO_2 nanocrystals, Nucl. Instrum. Methods Phys. Res. B Beam Interact. Mater. Atoms 409 (2017) 147–152.

[5] N. Pal, A. Sharma, V. Acharya, N.K. Chourasia, S. Biring, B.N. Pal, Gate Interface Engineering for Subvolt Metal Oxide Transistor Fabrication by Using Ion–Conducting Dielectric with Mn_2O_3 Gate Interface, ACS Appl. Electron. Mater. 2 (2020) 25–34.

[6] L. Wang, C. Hu, L. Shao, The antimicrobial activity of nanoparticles: present situation and prospects for the future, Int. J. Nanomedicine. 12 (2017) 1227–1249.

[7] R.K. Kunkalekar, M.S. Prabhu, M.M. Naik, A.V. Salker, Silver-doped manganese dioxide and trioxide nanoparticles inhibit both gram positive and gram negative pathogenic bacteria, Colloids Surf. B Biointerfaces 113 (2014) 429–434.

[8] K.S. Pugazhvadivu, K. Ramachandran, K. Tamilarasan, Synthesis and characterization of cobalt doped manganese oxide nanoparticles by chemical route, Phys. Procedia. 49 (2013) 205–216.

[9] R. Peng, N. Wu, Y. Zheng, Y. Huang, Y. Luo, P. Yu, L. Zhuang, Large-scale synthesis of metal-ion-doped manganese dioxide for enhanced electrochemical performance, ACS Appl. Mater. Inter. 8 (2016) 8474–8480.

[10] V. Hoseinpour, M. Souri, N. Ghaemi, Green synthesis, characterization, and photocatalytic activity of manganese dioxide nanoparticles, Micro Nano Lett 13 (2018) 1560–1563.

[11] C. Cheng, Y. Huang, N. Wang, T. Jiang, S. Hu, B. Zheng, H. Yuan, D. Xiao, Facile fabrication of Mn_2O_3 nanoparticle-assembled hierarchical hollow spheres and their sensing for hydrogen peroxide, ACS Appl. Mater. Inter. 7 (2015) 9526–9533.

[12] W. Tang, X. Shan, S. Li, H. Liu, X. Wu, Y. Chen, Sol-gel process for the synthesis of ultrafine MnO_2 nanowires and nanorods, Mater. Lett. 132 (2014) 317–321.

[13] B. Khodadadi, M. Bordbar, A. Yeganeh-Faal, Optical, structural, and photocatalytic properties of Cd-doped ZnO powders prepared via sol-gel method, J. Sol-Gel Sci. Technol. 77 (3) (2016) 521–527.

[14] M. Bordbar, S.M. Vasegh, S. Jafari, A. Yeganeh Faal, Optical and photocatalytic properties undoped and Mn-doped ZnO nanoparticles synthesized by hydrothermal method: Effect of annealing temperature, Iran. J. Catal. 5 (2) (2015) 135–141.

[15] M. Bordbar, S. Jafari, A. Yeganeh-Faal, B. Khodadadi, Influence of different precursors and Mn doping concentrations on the structural, optical properties and photocatalytic activity of single-crystal manganese-doped ZnO, J. Iran Chem Soc. 14 (4) (2017) 897–906.

[16] M. Abinaya, K. Govindan, M. Kalpana, K. Saravanakumar, S.L Prabavathi, V. Muthuraj, A. Jang, Reduction of hexavalent chromium and degradation of tetracycline using a novel indium-doped Mn_2O_3 nanorod photocatalyst, J. Hazard. Mater. 397 (2020) 122885.

[17] M. Chandra, S. Yadav, R. Rawat, K. Singh, Enhancement of magnetoelectric coupling in Cr doped Mn_2O_3, J. Phys. Condens. Matter. 32 (29) (2020) 295703.

[18] S. Esmael Balaghi, C.A. Triana, Greta R. Patzke, Molybdenum-Doped Manganese Oxide as a Highly Efficient and Economical Water Oxidation Catalyst, ACS Catal 10 (2020) 2074–2087.

[19] Jafar Hussain Shah, Mohammad Fiaz, Muhammad Athar, Jafar Ali, Mahnoor Rubab, Rashid Mehmood, Syed Umair Ullah Jamil, Ridha Djellabi, Facile synthesis of N/B-double-doped Mn_2O_3 and WO_3 nanoparticles for dye degradation under visible light, Environ. Technol. 41 (2019) 2372–2381.

[20] Maryam Qasim, Jianhua Hou, M.A. Qadeer, Sajid Butt, M. Hassan Farooq, M. Qasim Farooq, Faryal Idrees, M. Tanveer, Muhammad Tahir, Nitrogen-Doped Carbon Nanosheets Decorated With Mn_2O_3 Nanoparticles for Excellent Oxygen Reduction Reaction, Front. Chem. 7 (2019) 741.

[21] Subodh, Navin Kumar Mogha, Karan Chaudhary, Gyanendra Kumar, Dhanraj T. Masram, Fur-imine-functionalized graphene oxide-immobilized copper oxide nanoparticle catalyst for the synthesis of xanthene derivatives, ACS Omega 3 (11) (2018) 16377–16385.

[22] Subodh, Kunal Prakash, Dhanraj T. Masram, A reversible chromogenic covalent organic polymer for gas sensing applications, Dalton Trans 49 (2020) 1007–1010.

[23] Subodh, Prakash Kunal, Dhanraj T. Masram, Chromogenic covalent organic polymer- based microspheres as solid-state gas sensor, J. Mater. Chem. C. 8 (2020) 9201–9204.

[24] Subodh, Prakash Kunal, Karan Chaudhary, Dhanraj T. Masram, A new triazine–cored covalent organic polymer for catalytic applications, Appl. Catal. A-General 593 (2020) 117411.

[25] Deepika Yadav, A.K. Dixit, S. Raghothama, Satish Kumar Awasthi, Ni nanoparticle- confined covalent organic polymer directed diaryl-selenides synthesis, Dalton Trans 49 (2020) 12266–12272.

[26] Deepika Yadav, Satish Kumar Awasthi, A Pd confined hierarchically conjugated covalent organic polymer for hydrogenation of nitroaromatics: catalysis, kinetics, thermodynamics and mechanism, Green Chem 22 (2020) 4295–4303.

[27] Gyanendra Kumar, Navin Kumar Mogha, Manish Kumar, Dhanraj T.Masram Subodh, NiO nanocomposites/rGO as a heterogeneous catalyst for imidazole scaffolds with applications in inhibiting the DNA binding activity, Dalton Trans 49 (2020) 1963–1974.

[28] Deepika Yadav, Satish Kumar Awasthi, A Pd NP-confined novel covalent organic polymer for catalytic applications, New J. Chem. 44 (2020) 1320–1325.

[29] Karan Chaudhary, Subodh, Kunal Prakash, Navin Kumar Mogha Dhanraj T.Masram, Fruit waste (Pulp) decorated CuO NFs as promising platform for enhanced catalytic response and its peroxidase mimics evaluation, Arabian J. Chem. 13 (2020) 4869–4881.

[30] D. Ramarajan, P. Sivagurunathan, Effects of surfactants on morphology in synthesis of α-Mn_2O_3 nanostructures, J. Solid State Chem. 184 (2011) 597–600.

[31] Y. Chen, Y. Zhang, Q.Z. Yao, G.T. Zhou, S. Fu, H. Fan, Formation of α-Mn_2O_3 nanorods via a hydrothermal-assisted cleavage-decomposition mechanism, J. Solid State Chem. 180 (2007) 1218–1223.

[32] L. Liu, Z. Yang, H. Liang, H. Yang, Y. Yang, Shape- controlled synthesis of manganese oxide nanoplates by a polyol-based precursor route, Mater. Lett. 64 (2010) 891–893.

[33] J. Yu, L. Zhu, C. Fan, C. Zan, L. Hu, S. Yang, Q. Zhang, W. Zhu, L. Shi, F. Wei, Highly dispersed Mn_2O_3 microspheres: Facile solvothermal synthesis and their application as Li-ion battery anodes, Particuology 22 (2015) 89–94.

[34] S. Esmael Balaghi, C.A. Triana, Greta R. Patzke, Molybdenum-doped manganese oxide as a highly efficient and economical water oxidation catalyst, ACS Catalyst 10 (3) (2020) 2074–2087.

[35] Q. Li, Z.Li L.Yin, Y.Qi X.Wang, J. Ma, Copper doped hollow structured manganese oxide mesocrystals with controlled phase structure and morphology as anode materials for Lithium Ion Battery with improved electrochemical performance, ACS Appl. Mater. Interfaces 5 (2013) 10975–10984.

[36] Nasser A.M. Barakat, Ayman Yousef, M. Obaid, M.K.Tolba Gehan, Ag-doped Mn_2O_3 nanoflakes as effective catalyst for lignin liquefaction in supercritical methanol medium, Ceram. Int. 42 (2016) 4386–4392.

[37] K.S. Pugazhvadivua, K. Ramachandran, K. Tamilarasan, Synthesis and characterization of cobalt doped manganese oxide nanoparticles by chemical route, Physics Procedia 49 (2013) 205–216.

[38] Hamideh Darjazi, Saied Saeed Hosseiny Davarani, Hamid Reza Moazami, Taher Yousefi, Farideh Tabatabaei, Evaluation of charge storage ability of chrome doped Mn_2O_3 nanostructures derived by cathodic electrodeposition, Prog. Nat. Sci. Mater. Int. 26 (2016) 523–527.

[39] L. Jayaselvan, S. Thanka Rajan, C.Gnana Sambandam, Structural and phase analysis of pure and metal ion doped Mn_2O_3 nanoparticles prepared by microwave assisted sol-gel process, Rasayan J.Chem 13 (2020) 2223–2229.

[40] Manickavasagan Abinaya, Kadarkarai Govindan, Murugesan Kalpana, Karunamoorthy Saravanakumar, Seenivasan Laskhmi Prabavathi, Velluchamy Muthuraj, Am Jang, Reduction of hexavalent chromium and degradation of tetracycline using a novel indium-doped Mn_2O_3 nanorod photocatalyst, J. Hazard. Mater. 397 (2020) 122885.

[41] M. Karuppaiah, P. Sakthivel, S. Asaithambi, L.Krishna Bharat, Goli Nagaraju, Tansir Ahamad, K. Balamurugan, R. Yuvakkumar, G. Ravi, Elevated energy density and cycle stability of α-Mn_2O_3 3D-microspheres with addition of neodymium dopant for pouch-type hybrid supercapacitors, Electrochimica Acta 362 (2020) 137169.
[42] C. Karunakaran, A. Vijayabalan, G. Manikandan, Photocatalytic and bactericidal activities of hydrothermally synthesized nanocrystalline Cd-doped ZnO, Superlattices and Microstructures 51 (2012) 443–453.
[43] Karuna P. Ghoderao, Shweta N. Jamble, Rohidas B. Kale, Hydrothermally synthesized Cd-doped ZnO nanostructures with efficient sunlight-driven photocatalytic and antibacterial activity, J. Mater. Sci. Mater. Electron. 30 (12) (2019) 11208–11219.
[44] Dasari Ayodhya, Guttena Veerabhadram, One-pot green synthesis, characterization, photocatalytic, sensing and antimicrobial studies of Calotropis gigantea leaf extract capped CdS NPs, Mater. Sci. Eng. B 225 (2017) 33–44.
[45] Dasari Ayodhya, Guttena Veerabhadram, Facile fabrication, characterization and efficient photocatalytic activity of surfactant free ZnS, CdS and CuS nanoparticles, Journal of Science: Advanced Materials and Devices 4 (2019) 381–391.
[46] Gopi Somasundaram, Jayaprakash Rajan, P. Sangaiya, R. Dilip, Hydrothermal synthesis of CdO nanoparticles for photocatalytic and antimicrobial activities, Results in Materials 4 (2019) 100044.
[47] Karthik Kannan, D Radhika, Maria P. Nikolova, V. Andal, Kishor Kumar Sadasivuni, Sivarama Krishna Lakkaboyana, Facile microwave-assisted synthesis of metal oxide CdO-CuO nanocomposite: photocatalytic and antimicrobial enhancing properties, Optik 218 (2020) 165112.
[48] M. Karuppaiah, P. Sakthivel, S. Asaithambi, R. Murugan, G. Anandha babu, R. Yuvakkumar, G. Ravi, Solvent dependent morphological modification of micro-nano assembled Mn_2O_3/NiO composites for high performance supercapacitor applications, Ceram. Int. 45 (2019) 4298–4307.
[49] Y. Shao, B. Ren, H. Jiang, B. Zhou, L.V. Liping, J. Ren, L. Dong, J. Li, Z. Liu, Dual-porosity Mn_2O_3 cubes for highly efficient dye adsorption, J. Hazard. Mater. 333 (2017) 222–231.
[50] Florina Buciuman, Florin Patcas, Radu Craciun, Dietrich R.T. Zahn, Vibrational spectroscopy of bulk and supported manganese oxides, Phys. Chem. Chem. Phys. 1 (1999) 185–190.
[51] Muhamed Shareef Kolathodi, Samerender Nagam Hanumantha Rao, Tirupattur Srinivasan Natarajan, Gurpreet Singh, Beaded Manganese Oxide (Mn_2O_3) Nanofibers: Preparation and Application for Capacitive Energy Storage, J. Mater. Chem. A 4 (2016) 7883–7891.
[52] M.Y. Nassar, A.S. Amin, I.S. Ahmed, S. Abdallah, Sphere-like Mn_2O_3 nanoparticles: Facile hydrothermal synthesis and adsorption properties, J. Taiwan Inst. Chem. E. 64 (2016) 79–88.
[53] F. Li, C. Li, X. Liu, T. Bai, W. Dong, X. Zhang, Z. Shi, S. Feng, Microwave-assisted synthesis and up–down conversion luminescent properties of multicolor hydrophilic LaF_3:Ln^{3+} nanocrystals, Dalton Trans 42 (2013) 2015–2022.
[54] D. Komaraiah, E. Radha, J. Sivakumar, M.V. Ramana Reddy, R. Sayanna, Photoluminescence and photocatalytic activity of spin coated Ag+ doped anatase TiO_2 thin films, Optical Materials 108 (2020) 110401.
[55] K. Anandan, V. Rajendran, Influence of dopant concentrations (Mn = 1, 2 and 3 mol %) on the structural, magnetic and optical properties and photocatalytic activities of SnO_2 nanoparticles synthesized via the simple precipitation process, Superlattices and Microstructures 85 (2015) 185–197.
[56] K. Anandan; K. Rajesh, K. Gayathri, S.Vinoth Sharma, S.G. Mohammed Hussain, V. Rajendran, Effects of rare earth, transition and post transition metal ions on structural and optical properties and photocatalytic activities of zirconia (ZrO_2) nanoparticles synthesized via the facile precipitation process, Physica E 124 (2020) 114342.
[57] C.Maria Magdalane, K. Kaviyarasu, J.Judith Vijaya, C. Jayakumar, M. Maaza, B. Jeyaraj, Photocatalytic degradation effect of malachite green and catalytic hydrogenation by UV-illuminated CeO_2/CdO multilayered nanoplatelet arrays: investigation of antifungal and antimicrobial activities, J. Photochem. Photobiol. B Biol. 169 (2017) 110–123.
[58] F. Li, P. Wangyang, A. Zada, M. Humayun, B. Wang, Y. Qu, Synthesis of hierarchical Mn_2O_3 microspheres for photocatalytic hydrogen production, Mater. Res. Bull. 84 (2016) 99–104.
[59] S. Ravikumar, R. Gokulakrishnan, P. Boomi, In vitro antibacterial activity of the metal oxide nanoparticles against urinary tract infectious bacterial pathogens, Asian Pac, J. Trop. Dis. 1 (2012) 85–89.
[60] Y. Anwar, Antibacterial and lead ions adsorption characteristics of chitosan–manganese dioxide bionanocomposite, Int. J. Biol. Macromol. 111 (2018) 1140–1145.